



Precursor morphology-controlled formation of perovskites CaTiO_3 and their photo-activity for As(III) removal

Jiandong Zhuang^{a,*}, Qinfen Tian^{b,c}, Shan Lin^a, Wenbin Yang^a, Lihui Chen^a, Ping Liu^{b,*}

^a College of Materials Engineering, Fujian Agriculture and Forestry University, Fuzhou 350002, China

^b Research Institute of Photocatalysis, State Key Laboratory Breeding Base of Photocatalysis, Fuzhou University, Fuzhou 350002, China

^c Xi'an Catalyst Chemical Co., LTD, Northwest Institute for Nonferrous Metal Research, Xi'an 710016, China

ARTICLE INFO

Article history:

Received 28 September 2013

Received in revised form 29 January 2014

Accepted 8 February 2014

Available online 19 February 2014

Keywords:

CaTiO_3 nanoparticles
Controllable morphology
Photocatalysis
As(III) removal

ABSTRACT

CaTiO_3 nanoparticles (NPs) with diverse morphologies have been successfully synthesized by the precursor morphology-controlled formation based on a facile hydrothermal approach. The fabricated CaTiO_3 NPs were characterized by X-ray diffraction, field emission scanning electron microscope, high-resolution transmission electron microscopy, electron spin resonance, X-ray photoelectron spectra, and electrochemistry technology. It is found that the morphologies of as-synthesized CaTiO_3 NPs are strongly dependent on the aggregate status of the titania hydrogel precursors. Especially, the as-prepared CaTiO_3 NPs was, for the first time, used as the highly efficient photocatalysts to remove arsenite from aqueous solution. Due to their unique morphologies, the fern-like CaTiO_3 NPs exhibit a high photocatalytic activity toward the oxidation of As(III) (up to 98.4%) under irradiation. The photogenerated holes (h^+) are recognized as the primary active species responsible for As(III) oxidation. Meanwhile, a possible mechanism for the photo-oxidation of As(III) over CaTiO_3 has also been proposed.

© 2014 Elsevier B.V. All rights reserved.

1. Introduction

Arsenic contamination in natural water is posing a great threat to millions of people in many regions of the world [1]. As a widely distributed element in nature, arsenic can be mobilized into groundwater from soils and ores through both natural process and anthropogenic activities [2,3]. Chronic arsenic poisoning can cause lots of severe human health problems through contaminated drinking and agricultural irrigation water. In natural water, most arsenic pollution exists mainly as the As(III) and As(V) oxyanions (arsenite (AsO_2^-) and arsenate (AsO_4^{3-})). In comparison with arsenate, arsenite is much more toxic and mobile in natural waters, and less efficiently removed in traditional adsorption/coagulation processes [4,5]. Therefore, the oxidation of As(III) to As(V) is highly desirable for enhancing the immobilization of arsenic, which is also required for most arsenic removal technologies [6–8]. Photocatalysis provides a highly efficient approach for the oxidization of As(III), which

was first reported by Rajeshwar [6]. Since then, great efforts have been devoted to the development of the new photocatalysis-based technology to oxidize the As(III) [9–11].

In recent years, perovskite materials have received considerable attention for their phase transition due to their strong influence on their physical and chemical properties [12]. The perovskites exhibit a wide range of ferro-, piezo-, and pyro-electrical properties as well as electro-optical effects, which endow them with excellent performances as electronic, structural, magnetic, and refractory materials [13,15]. Moreover, the perovskites are also endowed with interesting chemical attributes due to their crystalline structure which can accommodate a spectrum of cations to yield defects or excess oxygen that would stabilize unstable oxidation states [16]. Consequently, they have been extensively used as heterogeneous catalysts for controlled partial hydrocarbon oxidation [17,18], gaseous pollutant removal [19–21], oxidative dehydrogenation of alkanes [22,23] and photocatalysis [24,25].

CaTiO_3 , 'the founding father' of the perovskite family, is one of most famous wide-gap oxides. The perovskite CaTiO_3 is of both fundamental interest and practical application importance in many disciplines such as mineralogy [26], materials sciences [27], electronic engineering [28], and even biotechnology [29] due to its unique structural characteristic, easy fabrication, high stability, and excellent biocompatibility. The low cost, facile synthesis and extraordinarily high chemical stability against acids

* Corresponding authors at: Fujian Agriculture and Forestry University, College of Materials Engineering, Fuzhou 350002, China; Fuzhou University, Research Institute of Photocatalysis, State Key Laboratory Breeding Base of Photocatalysis, Fuzhou 350002, China. Tel.: +86 591 83715175/+86 591 83779239; fax: +86 591 83715175/+86 591 83779239.

E-mail addresses: jdzhuang@gmail.com (J. Zhuang), liuping@fzu.edu.cn (P. Liu).

of CaTiO_3 also make it a promising photocatalyst in a moisture environment [30]. Importantly, cubic perovskite CaTiO_3 possesses a suitable conduction/valence band position for photocatalytic water splitting. Therefore, studies on the shape controllable synthesis of CaTiO_3 have attracted the great attention and have been extensive explored. Typically, CaTiO_3 is most commonly prepared via a solid-state reaction at temperatures of nearly 1350°C [31]. In addition, mechanochemical [32], peroxide routes [33], and hydrothermal [34] methods have also been developed to obtaining CaTiO_3 . To the best of our knowledge, however, no researches have been reported on the precursor morphology-controlled formation of CaTiO_3 NPs, not to mention their special photocatalytic activity to remove the arsenic.

Herein, we focus on a unique synthetic parameter, i.e., the influence of precursors, on the morphological evolution of calcium titanate under hydrothermal conditions. Three types of titanium precursors were employed to fabricate the well-defined CaTiO_3 NPs with diverse morphologies. Based on the finely tuned CaTiO_3 NPs, their performances for the photocatalytic removal of arsenic from aqueous solution has been systematically investigated. Under irradiation, all obtained CaTiO_3 NPs exhibit high photocatalytic activity in the oxidation of arsenite (AsO_3^{3-} to arsenate (AsO_4^{3-}). In particular, the arsenite (AsO_3^{3-}) removal efficiency based on CaTiO_3 photocatalysts is strongly dependent on their morphologies. The role of the active species during the photocatalytic oxidation of As(III) over CaTiO_3 has also been investigated in detail.

2. Experimental

2.1. Catalyst preparation

$\text{Ca}(\text{NO}_3)_2 \cdot 4\text{H}_2\text{O}$ and three kinds of titanium precursors [titanium tetrachloride (TiCl_4 , TTC), titanium isopropoxide ($\text{Ti}(\text{OC}_3\text{H}_7)_4$, TIP), and titanium *n*-butoxide ($\text{Ti}(\text{OC}_4\text{H}_9)_4$, TNB)] were used as the starting materials for the CaTiO_3 syntheses. All reagents are A.R. grade and used without further purification. In a typical synthesis, 0.02 mol TiCl_4 was added slowly into 300 mL of KOH solution (2 mol/L) under vigorous stirring. After stirring for 15 min at room temperature, the mixture was heated to boil for another 30 min to make sure the complete hydrolysis of titanium precursor. Then, the resulting white $\text{TiO}(\text{OH})_2$ hydrogel product were isolated by a centrifuge, washed with deionized water for 3 times to remove ionic remnants, and redispersion in 70 mL deionized water. Under vigorous stirring, 0.02 mol $\text{Ca}(\text{NO}_3)_2 \cdot 4\text{H}_2\text{O}$ was added into the suspension, and the pH value of the mixture was adjusted by using 2 mol/L KOH solution. After stirring for 30 min, the mixture was sealed into a Teflon-lined autoclave with a capacity of 100 mL, followed by hydrothermal treatment at 180°C for 12 h and then cooled down to room temperature naturally. The white precipitate deposited in the bottom of the autoclave was collected and isolated by a centrifuge, washed several time with deionized water and absolute ethanol, and dried at 60°C for further characterization. The as-prepared CaTiO_3 was denoted as Ca-TTC. By altering the titanium precursor, two other well-defined morphological features with distinct shapes of CaTiO_3 samples were also fabricated according to a similar procedure. The one obtained from TIP was denoted as Ca-TIP, and that obtained from TNB was denoted as Ca-TNB. A series of experiments with varying pH values were also carried out to optimize the synthesis condition.

2.2. Photocatalyst characterizations

The as-prepared samples were characterized by powder X-ray diffraction (XRD) on a Bruker D8 Advance X-ray diffractometer at 40 kV and 40 mA with Ni-filtered $\text{Cu K}\alpha$ radiation. Data were

recorded at a scan step width of 0.02° in the 2θ range of 10° to 70° . A nitrogen sorption-desorption experiment was carried out at 77 K using an ASAP2020 surface area and porosity analyzer (Micrometrics Instrument). Scanning electron microscopy (SEM) investigations were carried out on an FEI Nova NanoSEM 230 field-emission scanning electron microscope. The structure was investigated by transmission electron microscopy (TEM) and high-resolution TEM (HRTEM) on a FEI Tecnai G2F20S-TWIN microscope with a field-emission gun working at 200 kV. UV-vis diffuse reflectance spectra (UV-vis DRS) of the dry-pressed disk samples were obtained with a UV-vis spectrophotometer (Cary 500 scan spectrophotometers, Varian, USA) using BaSO_4 as a reflectance standard. X-ray photoelectron spectroscopy (XPS) analysis was conducted on an ESCALAB 250 photoelectron spectrometer (Thermo Fisher Scientific) at 1.2×10^{-9} mbar using an Al KR X-ray beam (1486.6 eV). A conventional three electrode cells using a ZENNIUM electrochemical workstation (Zahner, Germany) was used to determine the flat-band potential (V_{fb}) of the sample. The catalyst sample was deposited on a $1\text{ cm} \times 1\text{ cm}$ ITO conducting glass served as working electrode, while the Ag/AgCl electrode as the reference electrode and Pt as the counter electrode. The Mott-Schottky plot to evaluate the V_{fb} of the semiconductor space charge region was obtained by measuring impedance spectra at fixed frequency of 1 kHz. Electron spin resonance (ESR) spectra were obtained using Bruker model ESR 300E electron paramagnetic resonance spectrometer equipped with a quanta-Ray Nd:YAG laser system as the irradiation light source. The settings were center field, 3480.00 G; microwave frequency, 9.79 GHz; and power, 5.05 mW.

2.3. As(III) removal experiments

Stock solution (1 g/L) of arsenite [As(III)] was prepared by dissolving 1.734 g of NaAsO_2 into 1 L 20% HCl solution. The reaction solutions (2 mg/L AsO_2^-) used for the As(III) removal experiments were made by diluting the stock solution and adjusting the pH value to a near neutral state. In a typical As(III) removal experiment, 0.08 g of CaTiO_3 (Ca-TTC) was suspended in a quartz tube which contained 80 mL dilute arsenic solution. The tube was illuminated by four surrounding wide band lamps (4 W, Philips TL/05) with a predominant wavelength at 254 nm. During the experiment, the arsenic solution was stirred magnetically to ensure a good contact of CaTiO_3 with the arsenic species. To examine both the dark adsorption capability and the UV photoactivity of CaTiO_3 , the As(III) removal experiments were conducted with and without irradiation, respectively. For comparison, an As(III) photolysis process without catalysts was also performed under the same conditions. At the given irradiation time intervals, 1 mL of the suspension was collected, and then centrifuged to remove the photocatalyst. After recovering the photocatalyst by centrifugation, the pH value of the arsenic solution were adjusted to 4 through the dripping of concentrated HCl. Atomic fluorescence spectrometry (PF6, Beijing Pgeneral instrument Co., Ltd.) was used to analyze the As(III) content in the reaction solution. And the used photocatalyst was analyzed by XPS to indicate the chemical states of As after the photocatalytic reaction.

3. Results and discussion

3.1. XRD analysis and BET surface areas

It is well-known that the pH value plays important roles in controlling the crystal phases and sizes of the final products during the hydrothermal process. The XRD patterns of the resultant Ca-TTC products through the hydrothermal process at 180°C for 12 h under different pH values are shown in Fig. 1a. It is obvious that under a relatively low basic condition (pH = 10), the diffraction

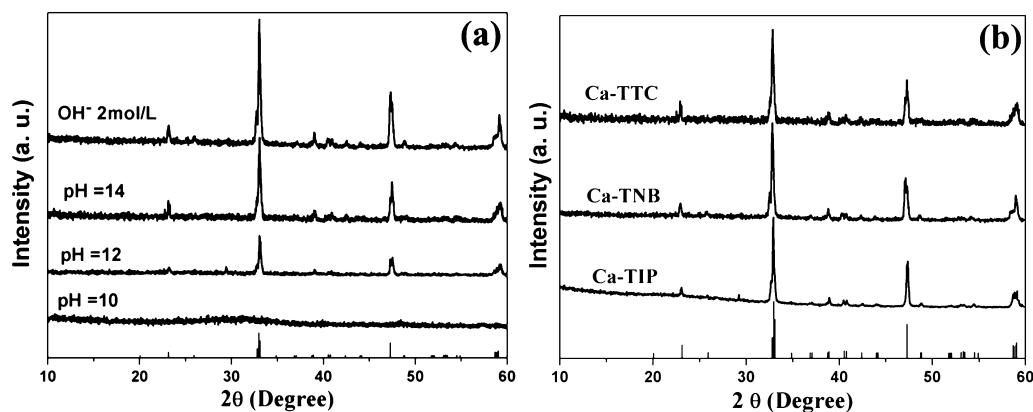


Fig. 1. Powder XRD patterns of the CaTiO_3 specimens produced with (a) different pH values by using TiCl_4 as titanium precursor, and (b) different titanium precursors at pH = 14. The bottom pattern with vertical bars is derived from the JCPDS card (No. 82-0299, space group $Pbnm$) of orthorhombic CaTiO_3 .

peaks of the sample are too wide and weak to be distinguished. While under strong basic conditions ($\text{pH} \geq 12$), the synthesized samples can be indexed to well-crystallized CaTiO_3 with relatively sharper diffraction peaks. The peak positions and relative intensities match well with the standard XRD data for orthorhombic CaTiO_3 (JSPDS card No. 82-0229, space group $Pbnm$), and peaks at 23.14° , 32.96° , 47.30° and 58.96° can be corresponded to the (1 1 0), (1 1 2), (2 2 0, 0 0 4) and (2 0 4) planes of the orthorhombic CaTiO_3 . Moreover, the intensity of the diffraction peaks significantly increases along with the elevation of the OH^- concentration, indicating that a strong basic condition is indispensable to facilitate the formation of CaTiO_3 NPs based on the fact that the formation of CaTiO_3 is a remarkable OH^- -consumed process. Herein, the optimum hydrothermal pH value is fixed to be 14 to facilitate the comparisons among diverse samples.

The crystal phases of the samples synthesized from different titanium precursors are also investigated. As shown in Fig. 1b, the CaTiO_3 samples synthesized from different precursors exhibit very similar XRD patterns (orthorhombic CaTiO_3). The intensive diffraction peaks indicate that these CaTiO_3 products are well-crystallized with relative large particle sizes. The average crystallite sizes of these three CaTiO_3 NPs are calculated via the Scherrer equation and summarized in Table 1.

3.2. Morphology and structure of the as-prepared CaTiO_3

The morphologies and microstructures of the CaTiO_3 NPs synthesized from different titanium precursors are further examined by FE-SEM and TEM. These micrographs depict that the morphology, particle size, as well as the aggregate status of the CaTiO_3 NPs significantly vary with different precursors. It can be clearly observed from Fig. 2a that a large number of CaTiO_3 cuboids with side length less than $1 \mu\text{m}$ can be uniformly generated by using TiCl_4 as precursor. The regular cuboid structure of CaTiO_3 can also be identified by the TEM image (Fig. 2b). Fig. 2c is the corresponding high-resolution (HR)-TEM image of Ca-TTC nano-cuboid, which exhibits clear lattice fringes. The interlayer spacings of 0.38 and 0.76 nm correspond to the (1 1 0) and (0 0 1) planes of CaTiO_3 , respectively. Moreover, the corresponding selected area electron

diffraction (SAED) pattern (lower-right inset in Fig. 2c) reveals the typical spot pattern of a well single-crystal structure of the sample.

When using TNB as titanium precursor, as shown in Fig. 3a, the size of the obtained CaTiO_3 cuboid particles is dramatically enlarged up to more than $2 \mu\text{m}$. Moreover, the surface of these cuboids sinks and ruptures to form step-like rectangular invagination hollow structure (lower left inset in Fig. 3a). This specific invagination structure endows the Ca-TNB sample a larger specific surface area as compared with the Ca-TTC sample. It can be seen from Table 1 that the BET surface area of Ca-TNB sample is $\sim 85.84 \text{ m}^2/\text{g}$, which is about 3 times that of the Ca-TTC sample (only $28.34 \text{ m}^2/\text{g}$).

Fig. 3c displays a low-magnification of SEM image of CaTiO_3 NPs fabricated from TIP (Ca-TIP NPs). It is interesting to note that the Ca-TIP NPs show a very different morphology as compared to the two former samples. Uniform fern-like CaTiO_3 NPs can be large-scale fabricated by using TIP as titanium precursor. The corresponding TEM image (upper right inset in Fig. 2c) further reveals this unique scale-work microstructure of the Ca-TIP NPs. Moreover, this fern-like CaTiO_3 sample possesses the largest BET specific surface area

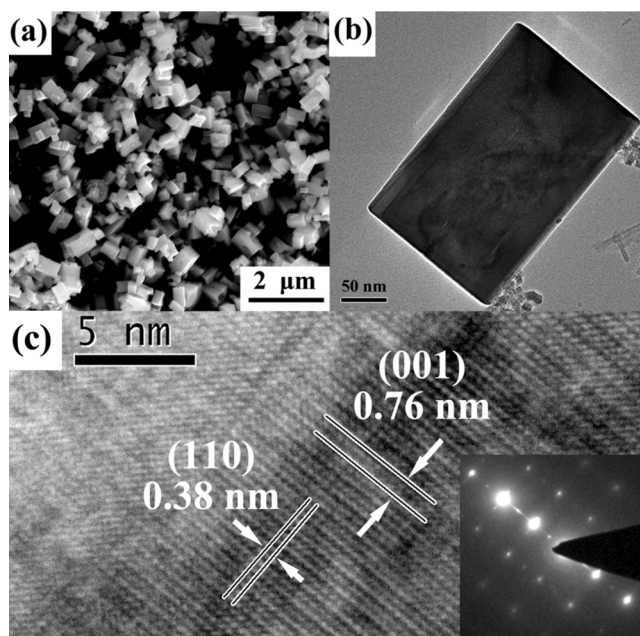


Fig. 2. (a) SEM image, (b) TEM image, and (c) HRTEM image and corresponding SAED pattern (inset) of the as-synthesized Ca-TTC sample.

Table 1
The crystalline size, BET area of the CaTiO_3 prepared from different Ti-precursors.

Ti-sources	Conditions	Crystallite size (nm)	S_{BET} (m^2/g)
TTC	180°C 12 h pH = 14	58.5	28.34
TNB	180°C 12 h pH = 14	61.1	85.84
TIP	180°C 12 h pH = 14	57.1	108.14

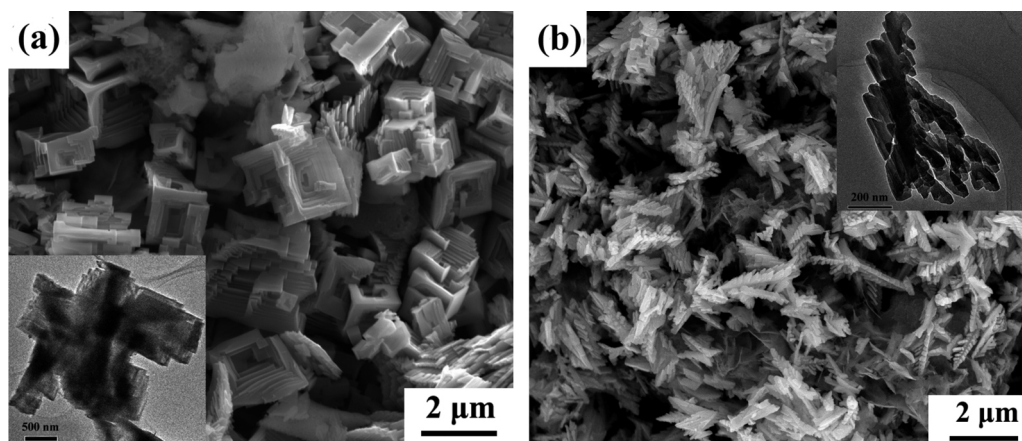


Fig. 3. SEM and TEM (inset) images of the CaTiO_3 specimens produced with different titanium precursors: (a) Ca-TNB and (b) Ca-TIP.

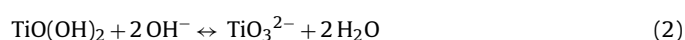
(up to $108.14 \text{ m}^2/\text{g}$) among these three CaTiO_3 samples, making it a potential photocatalyst for pollutant removal.

3.3. Tentative mechanism for the formation of CaTiO_3

Based on above systematic characterizations, it can be deduced that the size, shape, and dimensionality of as-prepared CaTiO_3 are significantly influenced by the varieties of titanium precursors. To further reveal the formation mechanism of CaTiO_3 , the effect of the morphologies of the titania hydrogels, which hydrolyzed from different titanium precursors, on the molding of CaTiO_3 NPs is discussed. Fig. 4a–c shows the SEM images of $\text{TiO}(\text{OH})_2$ hydrogels obtained by using TiCl_4 , TNB and TIP as the precursors, respectively. As shown in Fig. 4a, hydrolysis of TiCl_4 in KOH solution gives $\text{TiO}(\text{OH})_2$ NPs with uniform particle size of about 10 nm. Titania hydrogel has been proved to possess an enhanced reactivity relative to pure TiO_2 , and incorporation of Ca^{2+} in the titania hydrogel brings about heterogeneous nucleation of CaTiO_3 within the gel [35,36]. When the hydrothermal treatment is carried out at an appropriate temperature, isotropic etching of titania hydrogel by a basic solution and instant growth of CaTiO_3 in the presence of Ca ions can readily occur. Subsequently, CaTiO_3 NPs with regular cuboid structure are formed in the solution.

When titanium alkoxides are used as precursors, however, agglomerate hydrolysis products can be obtained. As shown in Fig. 4b, the hydrolysis of TNB forms compact massive titania hydrogel blocks, and the diameters are much larger than that hydrolyzed from TiCl_4 . Croker and co-workers [37] suggested that CaTiO_3 must crystallize from dissolved Ca species, and the rate determining step in the formation of CaTiO_3 occurs at the phase boundary (i.e., surface). Due to its massive structure, the etching and reaction process of titania hydrogel are blocked on the compact mass surface. Thus, the surface of these massive blocks is gradually etched, reacted and ruptured to form an invaginated structure.

While TIP is used as precursor, porous monolithic $\text{TiO}(\text{OH})_2$ hydrogel are obtained, as shown in Fig. 4c. Moreover, the porous monolith is apparently built from $\text{TiO}(\text{OH})_2$ NPs with diameter of several hundred nanometers. These NPs accumulate together to form a connected porous structure, which can improve the permeability of monolith. This special structure makes the Ca^{2+} ions and the $\text{TiO}(\text{OH})_2$ hydrogel in sufficient contact with each other, and provides adequate junctures to form fern-like CaTiO_3 NPs. The reaction of $\text{TiO}(\text{OH})_2$ and calcium ions to form calcium titanate in alkaline media can be represented by the following potential reaction schemes:



3.4. Photocatalytic properties of the CaTiO_3 product

The photocatalytic activity of the as-prepared CaTiO_3 samples and some comparative experiments were evaluated and conducted by removal of As(III) in aqueous suspension under UV-254 nm irradiation. The temporal changes in the concentration of As(III) over CaTiO_3 under different experimental conditions are shown in Fig. 5. Fig. 5a shows the adsorption capabilities of these three samples in the dark condition. After 40 min of dark adsorption, the removal amounts of As(III) over Ca-TTC, Ca-TNB and Ca-TIP samples are examined to be 39.2%, 70.5% and 84.7%, respectively. This result indicates the As(III) species can available adsorb on the CaTiO_3 surface, and the adsorption capability is close related with the specific surface area of CaTiO_3 NPs (Fig. S1). Obviously, due to its unique morphology and largest specific surface area, Ca-TIP sample exhibits the strongest adsorbility among these three samples, suggesting the Ca-TIP NPs can work as an efficient absorbent for As(III) removal.

The photocatalytic removal of As(III) assisted by CaTiO_3 is shown in Fig. 5b. Curve D shows the photolysis of As(III). No appreciable change in concentration of As(III) is observed after 40 min of irradiation, indicating that As(III) is stable in the absence of photocatalyst. When assisted by CaTiO_3 powders under UV irradiation, the concentrations of As(III) decline rapidly. All three samples exhibit superior activity for the removal of As(III) from aqueous solution. After irradiation for 40 min, the removal ratios of As(III) over Ca-TTC, Ca-TNB and Ca-TIP samples are up to 83.2%, 93.6% and 98.4%, respectively. Additionally, the As(III) removal rate are obviously accelerated as compared with that in the dark condition.

In order to reveal the reaction process of As(III) on the catalyst surface, XPS were used to investigate the chemical states of the As species adsorbed on the Ca-TIP photocatalyst before and after reaction. The detailed spectra of As 3d are presented in Fig. 6. Two characteristic peaks of As 3d can be observed evidently, and the peaks located at about 44.6 eV and 45.7 eV can be assigned to As(III) and As(V), respectively [38]. Before irradiation, as shown in Fig. 6a, As(III) is the main arsenic species on the photocatalyst surface. A small amount of As(V) can also be found in the XPS spectrum since it is unavoidable to expose the sample to the light and air. It should be noted that the XPS spectrum (Fig. 6b) of the sample shows a radical change after the photocatalytic reaction. The intensity of As(V) peak is dramatically strengthened while that of As(III) peak

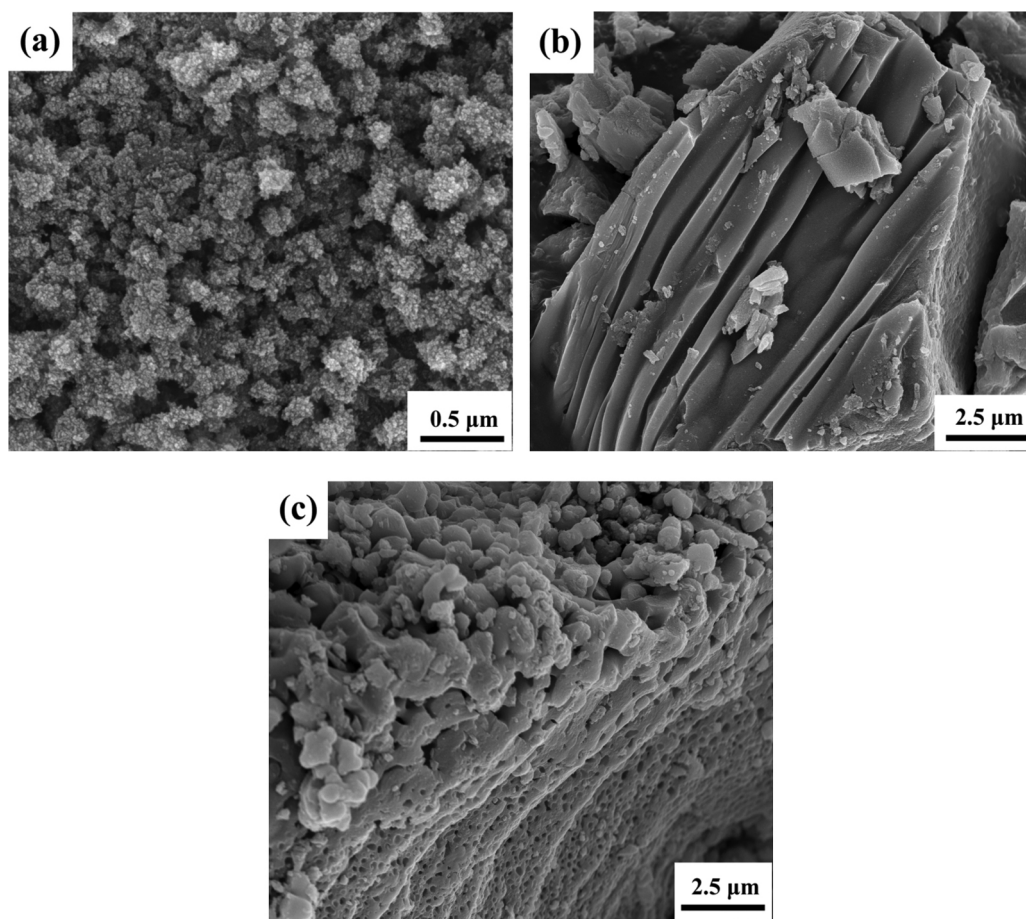


Fig. 4. SEM images of the TiO_2 hydrogel obtained from different titanium precursors: (a) TiCl_4 , (b) TNB and (c) TIP.

shows a distinct diminution. Through analysis of the ratio of these two peak areas, the ratio of As(V) to As(III) is calculated to be 5.2:1. This result indicates that the CaTiO_3 nanomaterials can not only photo-oxidize As(III) to As(V) efficiently, but also adsorb the As(V) species lightly (Fig. S2). Therefore, due to the high efficiencies in As(III) oxidation and As(V) adsorption, the CaTiO_3 is proposed to be a promising photocatalyst for As(III) oxidation and removal.

3.5. Optical properties and electric band structure of CaTiO_3

The optical properties of CaTiO_3 have been studied by UV–vis diffuse reflectance spectroscopy, and the corresponding UV–vis diffuse reflectance absorption spectrum $F(R)$ is shown in Fig. 7. The

relation between the absorption coefficient and band gap energy for a direct gap semiconductor can be described by the formula: $[F(R)E]^2 = A(E - E_g)$, where E and E_g are photon energy and optical band gap energy, respectively, and A is the characteristic constant of the semiconductor. In the equation, $[F(R)E]^2$ has a linear relation with E . Extrapolating the linear relation to $[F(R)E]^2 = 0$ gives the band gap E_g of the sample. As shown in Fig. 3 (inset), the band gap of CaTiO_3 is approximately 3.65 eV, corresponding to an optical absorption edge of 340 nm.

It is well known that the electric band structure of a semiconductor is the foundation for exploring its photocatalytic mechanism. The conduction band potential (E_{CB}) of n-type semiconductor is very close to the flat-band potential (V_{fb}) [39]. Herein, we used an

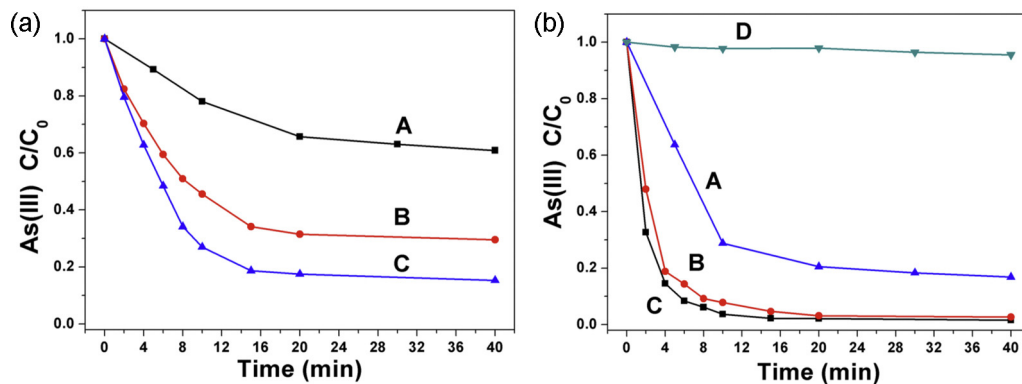


Fig. 5. Temporal changes in the concentration of As(III) with various photocatalysts under different experimental conditions: (a) in the dark and (b) with UV-254 nm irradiation. (A) Ca-TTC, (B) Ca-TNB, (C) Ca-TIP and (D) No photocatalyst.

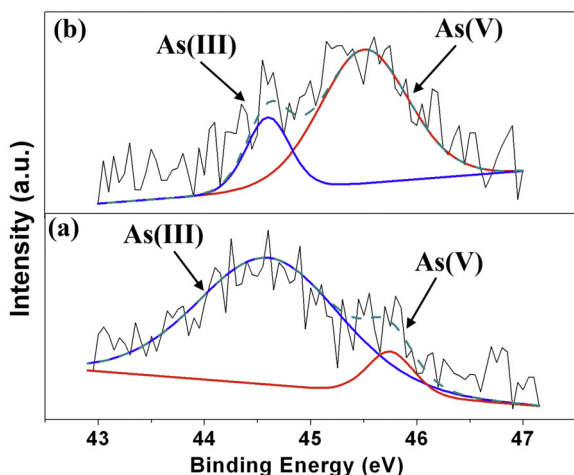


Fig. 6. As 3d XPS spectra of Ca-TiP photocatalysts, (a) before irradiation, (b) after reaction.

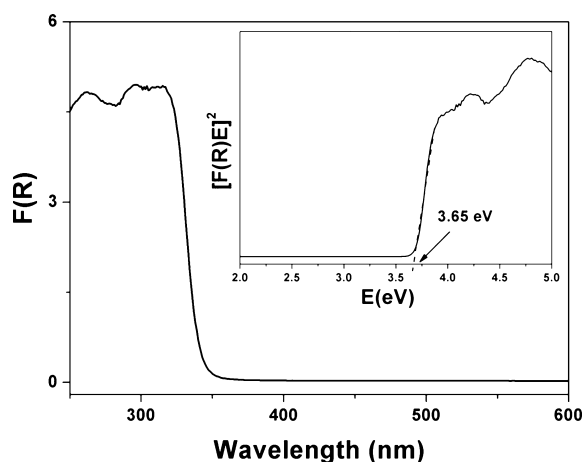


Fig. 7. UV-vis diffuse reflectance spectrum of CaTiO_3 , with the optical band gap energy E_g (inset).

electrochemical method to measure the V_{fb} of the CaTiO_3 semiconductor [40]. Fig. 8a shows typical Mott-Schottky plots in the dark for CaTiO_3 . The positive slope of the linear C^{-2} - E plot suggests the expected n-type semiconductor of CaTiO_3 [41]. Another important parameter derived from the measurement is the V_{fb}

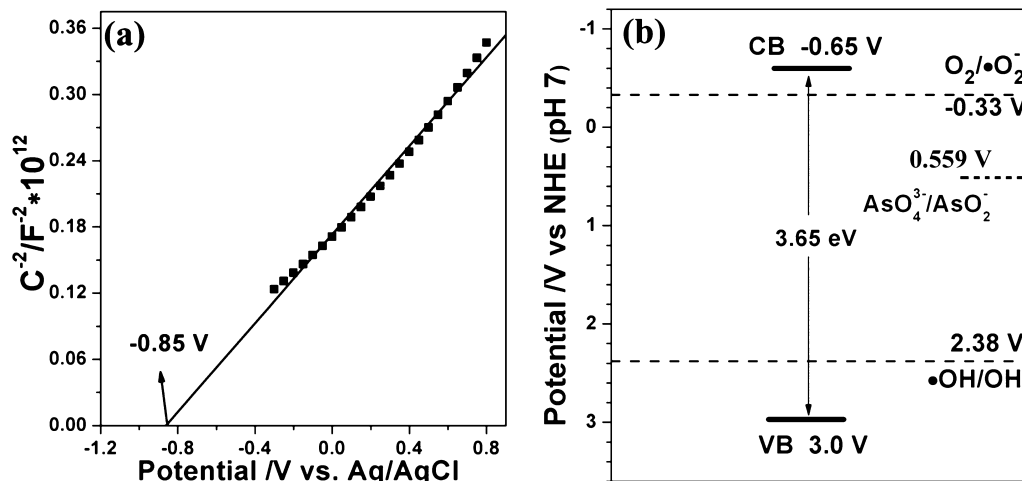


Fig. 8. (a) Mott-Schottky plots and (b) band structure of CaTiO_3 NPs.

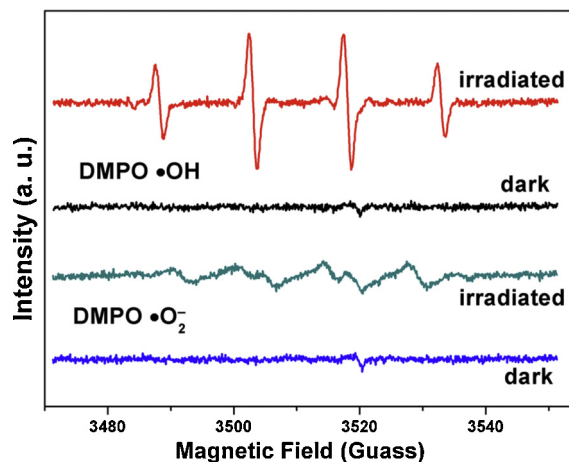


Fig. 9. DMPO spin-trapping ESR spectra of CaTiO_3 (Ca-TTC) in aqueous dispersion for $\text{DMPO}\cdot\text{OH}$ and in methanol dispersion for $\text{DMPO}\cdot\text{O}_2^{\cdot-}$, respectively.

value, which obtained by extrapolation of the Mott-Schottky plots is roughly -0.85 V versus Ag/AgCl at $\text{pH} = 7$ (equivalent to -0.65 V vs. NHE at $\text{pH} = 7$). Therefore, it can be determined that the E_{CB} of CaTiO_3 is about -0.65 V (Fig. 8b). According to the band gap energy ($E_g = 3.65$ eV) obtained from UV-vis DRS measurement, the value band potential (E_{VB}) of CaTiO_3 is deduced to be about 3.0 V. In addition, also shown in the same energy diagram are the standard redox potentials for the $\text{AsO}_4^{3-}/\text{AsO}_2^{\cdot-}$ redox couples (0.559 V vs. NHE) extracted from the literature [42]. It is obviously that the photo-generated carriers will have sufficient energy to oxidize As(III) to As(V) in the solution.

3.6. Photooxidation mechanism of As(III) over CaTiO_3

The photooxidation of As(III) could be mainly assigned to some active species, such as $\cdot\text{OH}$, $\cdot\text{O}_2^-$ and photogenerated hole (h_{vb}^+). ESR spectroscopy is a widely used method for the detection of relatively stable free radicals. For the photocatalysis system, the photogenerated holes on irradiated photocatalysts can oxidize H_2O or OH^- to give $\cdot\text{OH}$, while the photogenerated electrons can reduce O_2 to give $\cdot\text{O}_2^-$. In order to identify the reactive species responsible for As(III) photooxidation, $\text{CaTiO}_3/\text{DMPO}$ systems were examined by ESR. As shown in Fig. 9, six characteristic peaks from the $\text{DMPO}\cdot\text{O}_2^{\cdot-}$ species can be observed in CaTiO_3 methanolic dispersion, and four characteristic peaks of $\text{DMPO}\cdot\text{OH}$ can also be

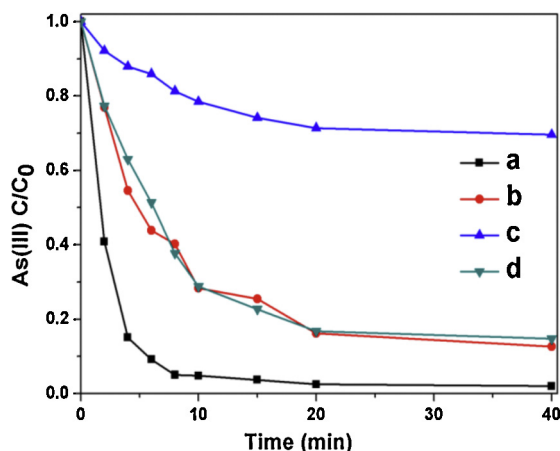
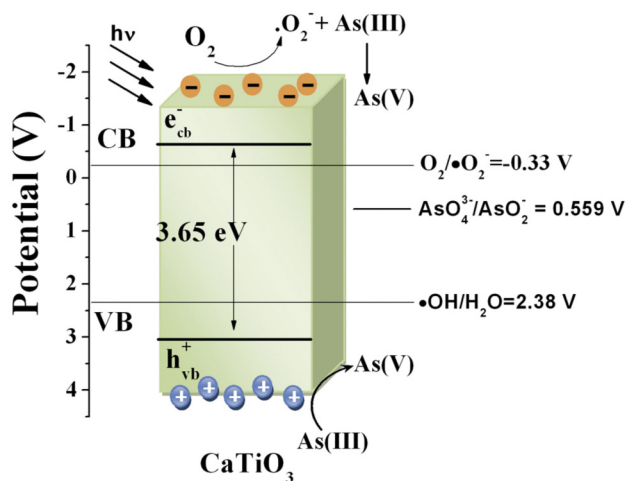


Fig. 10. Photoinduced removal profile of As(III) over Ca-TTC with (a) 0.1 g $\text{Cu}(\text{NO}_3)_2 \cdot 5\text{H}_2\text{O}$, (b) 2 mL isopropanol, (c) 0.1 g ammonium oxalate, and (d) without any scavenger.

obviously observed in the irradiated CaTiO_3 suspension. This result is a strong evidence that the photogenerated charge carriers in a CaTiO_3 photocatalyst not only possess a good separation efficiency of the photogenerated hole and electron, but also are long-lived enough to react with the surface adsorbed O_2 or H_2O , suggesting that the CaTiO_3 can serve as a effective photocatalyst for the photooxidation of As(III). Moreover, the intensity difference between DMPO- $\bullet\text{OH}$ signals and DMPO- $\bullet\text{O}_2^-$ signals demonstrates that there is an obvious contrast between the reactivity of photogenerated holes (h_{vb}^+) and electrons (e_{cb}^-) in the irradiated CaTiO_3 . We infer that this phenomenon is in close relationship with the electric band structure of CaTiO_3 . As shown in Fig. 8b, the potential fall between E_{VB} and $E(\bullet\text{OH}/\text{H}_2\text{O})$ is larger than that between E_{CB} and $E(\text{O}_2/\bullet\text{O}_2^-)$, leading to a higher activity of h_{vb}^+ than that of e_{cb}^- .

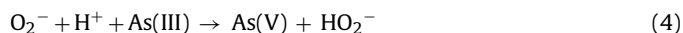
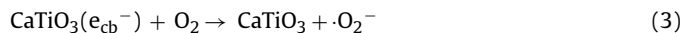
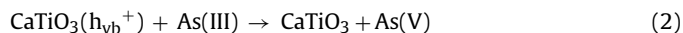
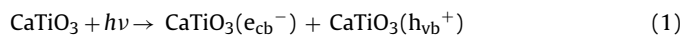
In order to make clear that the role of the photoinduced holes plays the role on the production of $\bullet\text{OH}$ radicals and the photooxidation of As(III) over CaTiO_3 , photocatalytic oxidation of As(III) in aqueous CaTiO_3 suspension was conducted in the presence of different scavengers. Isopropanol has been described as the best hydroxyl radical quencher because of its high-rate-constant reaction with the $\bullet\text{OH}$ radical [43], and ammonium oxalate (AO) can act as an efficient hole scavenger [44]. They have been widely used in photocatalysis in order to discriminate the direct oxidation of substrates by holes or by $\bullet\text{OH}$ radicals [45,46]. Fig. 10 summarizes the time-dependent removal of As(III) over CaTiO_3 with different scavengers addition. After the addition of isopropanol, no obvious changing was found in the removal profile of As(III), demonstrating the $\bullet\text{OH}$ radical is not a main active species causing As(III) oxidation. Nevertheless, when the AO was added into the system, the photooxidation process of As(III) was remarkably inhibited, and the removal efficiency of As(III) over CaTiO_3 was retarded from 85.3% to 30.4%. Thus, these evidences lead to the conclusion that the photogenerated hole (h_{vb}^+) should be the main factor that responsible for As(III) oxidation in this system. In order to be more specific regarding the effect of h_{vb}^+ , 0.1 g of $\text{Cu}(\text{NO}_3)_2$ was also added into the photocatalytic system. It is evident that Cu(II) ions can act as a electron scavenger that will reduce the recombination rate of photogenerated hole–electron pairs [47]. As shown in Fig. 10, the photoinduced removal efficiency of As(III) over CaTiO_3 is promoted (from 85.3% to 98.1%) by adding Cu(II) ions, confirming the h_{vb}^+ is largely responsible for the oxidation of As(III).

On the basis of the experimental results mentioned above, a possible photocatalytic process (Scheme 1 and Eqs. (1)–(4)) for the photooxidation of As(III) in the UV light irradiated CaTiO_3



Scheme 1. Proposed mechanism for the UV light photocatalytic reaction of As(III) over CaTiO_3 .

system could be concluded as follows: under UV light irradiation, the CaTiO_3 NPs are excited to form the photogenerated electron–hole pairs (Eq. (1)). The valence band potential (E_{VB}) of CaTiO_3 (3.00 V) is much more positive than $E_0(\bullet\text{OH}/\text{H}_2\text{O})$ (2.38 V vs. NHE), the holes can theoretically oxidize the hydroxyl group to produce $\bullet\text{OH}$ radicals. However, since the CaTiO_3 can absorb As(III) species available, the holes may directly oxidize the As(III) absorbed on the photocatalyst surface instead (Eq. (2)). In addition, the excited electrons in the conduction band can reduce O_2 to produce oxidant $\bullet\text{O}_2^-$ radicals (Eq. (3)), since the E_{CB} of CaTiO_3 (-0.65 V) is more negative than $E_0(\text{O}_2/\bullet\text{O}_2^-)$ (-0.33 V vs. NHE) [48]. Then the produced $\bullet\text{O}_2^-$ radicals can also oxidize As(III) to form As(V) [49], as shown in Eq. (4). In a word, the high photocatalytic activity of CaTiO_3 for As(III) oxidation may be mainly attributed to the active species, photogenerated holes (h^+) and $\bullet\text{O}_2^-$. The above-mentioned reactions could be described by the following equations:



4. Conclusion

In summary, CaTiO_3 NPs with diverse morphologies have been successfully synthesized from three different titanium precursors via a facile hydrothermal method. The morphology of achieved CaTiO_3 NPs can be readily molded by controlling the morphology of initial titania hydrogel. Importantly, the CaTiO_3 NPs can be used as highly efficient photocatalysts to remove the arsenic species from aqueous solution. Due to its unique morphology and large specific surface area, the fern-like CaTiO_3 sample exhibits an excellent photocatalytic activity for As(III) removal (up to 98.4%) in aqueous solution under UV-254 nm irradiation. The mainly active species responsible for the oxidation of As(III) are detected and determined to be photogenerated holes (h^+) and $\bullet\text{O}_2^-$. By analyzing the electric band structure of CaTiO_3 , a reasonable mechanism for the photooxidation of As(III) over CaTiO_3 has been proposed. Based on the unique morphologies, special nanostructures and excellent photocatalytic performance, the elaborately fabricated CaTiO_3 NPs may serve as a promising efficient photocatalyst in water purification to address the severe environmental issues nowadays.

Acknowledgments

The authors are indebted to Dr. Yu Chen for his great help in preparing this paper. The work is supported by National Natural Science Foundation of China (21303244, 21173046), National Basic Research Program of China (973 Program: 2010CB234604), Technological Innovation Fund of Shanghai Institute of Ceramic (Y21ZC8180G), and Open Fund of Fujian Provincial Key Laboratory of Photocatalysis—State Key Laboratory Breeding Base in Fuzhou University.

Appendix A. Supplementary data

Supplementary data associated with this article can be found, in the online version, at <http://dx.doi.org/10.1016/j.apcatb.2014.02.015>.

References

- [1] M. Amini, K. Mueller, K.C. Abbaspour, T. Rosenberg, M. Afyuni, K.N. Moller, M. Sarr, C.A. Johnson, *Environmental Science and Technology* 42 (2008) 3662–3668.
- [2] A.H. Welch, D. Westjohn, D.R. Helsel, R.B. Wanty, *Ground Water* 38 (2000) 589–604.
- [3] P.L. Smedley, D.G. Kinniburgh, *Applied Geochemistry* 17 (2002) 517–568.
- [4] H. Lee, W. Choi, *Environmental Science and Technology* 36 (2002) 3872–3878.
- [5] Y. Kim, C. Kim, I. Choi, S. Rengaraj, J. Yi, *Environmental Science and Technology* 38 (2004) 924–931.
- [6] H. Yang, W.Y. Lin, K. Rajeshwar, *Journal of Photochemistry and Photobiology A: Chemistry* 123 (1999) 137–143.
- [7] M.T. Emmett, G.H. Khoe, *Water Research* 35 (2001) 649–656.
- [8] U.S. Environmental Protection Agency, *Arsenic in Drinking Water*, Washington, DC (2000).
- [9] J. Ryu, W. Choi, *Environmental Science and Technology* 38 (2004) 2928–2933.
- [10] Q. Tian, J. Zhuang, J. Wang, P. Liu, *Applied Catalysis A: General* 425 (2012) 74–78.
- [11] H. Cui, Y. Su, Q. Li, S. Gao, J.K. Shang, *Water Research* 47 (2013) 6258–6268.
- [12] M. Pena, J. Fierro, *Chemical Reviews* 101 (2001) 1981–2018.
- [13] P. Lacorre, F. Goutenoire, O. Bohnke, R. Retoux, Y. Laligant, *Nature* 404 (2000) 856–858.
- [15] H. Tanaka, M. Misono, *Current Opinion in Solid State and Materials Science* 5 (2001) 381–387.
- [16] T. Shimizu, *Catalysis Reviews* 34 (1992) 355–371.
- [17] W. Libby, *Science* 171 (1971) 499–500.
- [18] H. Zhou, J. Guo, P. Li, T. Fan, D. Zhang, J. Ye, *Scientific Reports* 3 (2013) 1667.
- [19] R.D. Zhang, N. Luo, W. Yang, N. Liu, B.H. Chen, *Journal of Molecular Catalysis A: Chemical* 371 (2013) 86–93.
- [20] J. Zhu, A. Thomas, *Applied Catalysis B: Environmental* 92 (2009) 225–233.
- [21] G. Valderrama, C.U. de Navarro, M.R. Goldwasser, *Journal of Power Sources* 234 (2013) 31–37.
- [22] R. Watanabe, Y. Sekine, J. Kojima, M. Matsukata, E. Kikuchi, *Applied Catalysis A: General* 398 (2011) 66–72.
- [23] R. Watanabe, Y. Sekine, M. Matsukata, E. Kikuchi, *Catalysis Letters* 131 (2009) 54–58.
- [24] S. Pokrant, A.E. Maegli, G.L. Chiarello, A. Weidenkaff, *CHIMIA International Journal for Chemistry* 67 (2013) 162–167.
- [25] Q. Fu, J. Li, T. He, G. Yang, *Journal of Applied Physics* 113 (2013) 104303–104307.
- [26] M.S. Hu, H.R. Wenk, D. Sinityna, *American Mineralogist* 77 (1992) 359–373.
- [27] X. Yang, J. Fu, C. Jin, J. Chen, C. Liang, M. Wu, W. Zhou, *Journal of the American Chemical Society* 132 (2010) 14279–14287.
- [28] X. Wang, C.N. Xu, H. Yamada, K. Nishikubo, X.G. Zheng, *Advanced Materials* 17 (2005) 1254–1258.
- [29] A.P. Rodriguez, M. Inoue, T. Tanaka, M. Miyake, A.M. Sfer, E. Kishimoto, H. Tsujigawa, R.S. Rivera, H. Nagatsuka, *Journal of Biomedical Materials Research, Part A* 93 (2010) 297–303.
- [30] H. Kim, D. Hwang, Y. Kim, J. Lee, *Chemical Communications* (1999) 1077–1078.
- [31] S.A. Redfern, *Journal of Physics: Condensed Matter* 8 (1996) 8267.
- [32] I.R. Evans, J.A. Howard, T. Sreckovic, M.M. Ristic, *Materials Research Bulletin* 38 (2003) 1203–1213.
- [33] G. Pfaff, *Journal of Materials Chemistry* 2 (1992) 591–594.
- [34] M.M. Lencka, R.E. Riman, *Chemistry of Materials* 7 (1995) 18–25.
- [35] T. Kutty, R. Vivekanandan, *Materials Letters* 5 (1987) 79–83.
- [36] T. Kutty, R. Vivekanandan, P. Murugaraj, *Materials Chemistry and Physics* 19 (1988) 533–546.
- [37] D. Croker, M. Loan, B. Hodnett, *Crystal Growth and Design* 9 (2009) 2207–2213.
- [38] H. Nesbitt, G. Canning, G. Bancroft, *Geochimica et Cosmochimica Acta* 62 (1998) 2097–2110.
- [39] S.R. Morrison, *Electrochemistry at semiconductor and oxidized metal electrodes*, Plenum Press, New York, (Chapter 4) (1980).
- [40] R. Ramesham, *Thin Solid Films* 322 (1998) 158–166.
- [41] V. Spagnol, E. Sutter, C. Debiemme-Chouvy, H. Cachet, B. Baroux, *Electrochimica Acta* 54 (2009) 1228–1232.
- [42] A. J. Bard, R. Parsons, J. Jordan (Eds.), *Standard Potentials in Aqueous Solution*, Marcel Dekker, New York, (1985).
- [43] Y. Chen, S. Yang, K. Wang, L. Lou, *Journal of Photochemistry and Photobiology A: Chemistry* 172 (2005) 47–54.
- [44] H. Kominami, A. Furusho, S. Murakami, H. Inoue, Y. Kera, B. Ohtani, *Catalysis Letters* 76 (2001) 31–34.
- [45] A. Amine-Khodja, A. Boulkamh, C. Richard, *Applied Catalysis B: Environmental* 59 (2005) 147–154.
- [46] J. Zhuang, W. Dai, Q. Tian, Z. Li, L. Xie, J. Wang, P. Liu, X. Shi, D. Wang, *Langmuir* 26 (2010) 9686–9694.
- [47] S.H. Yoon, J.H. Lee, *Environmental Science and Technology* 39 (2005) 9695–9701.
- [48] Z. Li, T. Dong, Y. Zhang, L. Wu, J. Li, X. Wang, X. Fu, *The Journal of Physical Chemistry C* 111 (2007) 4727–4733.
- [49] J. Ryu, W. Choi, *Environmental Science and Technology* 40 (2006) 7034–7039.